PCCP

Modification of ultrathin C60 interlayer on electronic structure and molecular packing of C8-BTBT on HOPG

Journal:	*Physical Chemistry Chemical Physics*
Manuscript ID	CP-ART-08-2020-004288.R1
Article Type:	Paper
Date Submitted by the Author:	05-Oct-2020

Complete List of Authors:	Zhao, Yuan; Central South University, Hunan Key Laboratory for Super-microstructure and Ultrafast Process,College of Physics and Electronics liu, xiaoliang; central south university, Li, Lin; Central South University of Forestry and Technology, School of Electronics and Information Engineering, Central South University of Forestry and Technology, Changsha, 410004, P. R. China. Wang, Shitan; Central South University, Li, Youzhen; Central South University, School of Physics and Electronics Xie, Haipeng; Central South University Niu, Dongmei; Central South University Huang, Han; Central South University, School of Physics and Electronics; Gao, Yongli; University of Rochester,

Modification of ultrathin C_{60} interlayer on electronic structure and molecular packing of C8-BTBT on HOPG

Yuan Zhao,[a] Xiaoliang Liu,[b*] Lin Li,[c] Shitan Wang,[a] Youzhen Li,[a] Haipeng Xie,[a] Dongmei Niu,[a] Han Huang,[a] Yongli Gao[c]

[a]School of Physics and Electronics, Central South University, Changsha, 410083, P. R. China

[b]School of Electronics and Information Engineering, Central South University of Forestry and Technology, Changsha, 410004, P. R. China

[c]Department of Physics and Astronomy, University of Rochester, Rochester, New York 14627, United States

Abstract

X-ray photoelectron spectroscopy (XPS), ultraviolet photoelectron spectroscopy (UPS), atomic force microscopy (AFM) and X-ray diffraction (XRD) were applied to investigate the electronic structure, molecular packing of C8-BTBT on HOPG with an ultrathin C_{60} interlayer. It is found that C8-BTBT displays a Vollmer-Weber (V-W) growth mode on HOPG with an ultrathin C_{60} interlayer (0.7 nm). Compared to the uniform lying-down growth mode as directly grown on HOPG, the C8-BTBT molecules here adopt a lying-down orientation at low coverage with some small tilt angles because the π-π interaction between C8-BTBT and HOPG is partly disturbed by the C_{60} interlayer, delivering a higher HOMO in C8-BTBT. An interface dipole of 0.14 eV is observed due to electron transport from C8-BTBT to C_{60}. The upward and downward band bending in C8-BTBT and C_{60}, respectively, near the C8-BTBT/C_{60} interface can reduce the hole transport barrier at the interface, facilitating the hole injection from C_{60} to C8-BTBT, while a large electron transfer barrier from C_{60} to C8-BTBT is detected at this interface, which can effectively limit electron injection from C_{60} to C8-BTBT. The HOMO of C8-BTBT near the interface is largely lifted up by the C_{60} insertion layer which causes a p-doping effect and increases the hole mobility in C8-BTBT. Furthermore, owing to the LUMO of C_{60} residing in gap of C8-BTBT, charge transfer can occur between the C_{60} and the trap states in C8-BTBT to effectively passivate the trapping states. Our efforts help to better understand the electron structure and film growth of anisotropy molecules and provide a useful strategy to improve performance of C8-BTBT-based devices.

Keywords: PES, AFM, C8-BTBT, electronic structure, OFETs.

1. Introduction

In the past few decades, organic semiconductors (OSCs) have attracted considerable interests due to their particular characteristics compared to inorganic semiconductors [1, 2]. Their potential applications in electronic devices include organic light-emitting diodes (OLEDs)[3, 4], organic field-effect transistors (OFETs)[5-7], organic photovoltaic cells (OPVs)[8, 9] and organic spintronics[10, 11]. Among various OSCs, as a derivative of benzothieno[3,2-b]benzothiophene (BTBT) core structure, 2,7-diocty[1] benzothieno[3,2-b]benzothiophene (C8-BTBT) has been considered as a promising OSC in organic electronic devices, especially in OFETs due to its excellent carrier mobility, high air stability and easy synthesis[12, 13]. As shown in the inset of Fig. 1, the intermolecular exchange of π-electrons of BTBT core in normal direction of self-assembly C8-BTBT contributes to the high mobility of C8-BTBT. Mineawari et al. prepared C8-BTBT films with high crystallinity using inkjet printing, achieving a mobility of 16.4 $cm^2V^{-1}s^{-1}$[14]. A record-breaking mobility of up to 43 $cm^2V^{-1}s^{-1}$ reported by Yuan et al. in the C8-BTBT thin film transistor, stirring up an upsurge in the exploration of C8-BTBT[15]. So far, a lot of efforts have been spent on exploring the applications of C8-BTBT. In He et al.'s report, intrinsic hole mobility over 30 $cm^2V^{-1}s^{-1}$, band-like transport down to 150 K and Ohmic contact with 100 Ω·cm was demonstrated in an ultimate C8-BTBT monolayer based OTFT[16]. By structuring heterojunction based on the $CH_3NH_3PbI_3$/C8-BTBT interface, Tong et al. fabricated photodetectors with a ratio of photocurrent to dark current as high as 2.4×10^4 and a fast response of about 4.0 ms[17]. Owing to the coexistence of an ultra-long spin lifetime and the band-like transport in BTBT-based single crystal, a micrometer-scale spin diffusion length was found by Tsurumi et al[18].

As one of the most key factors to achieve better device performance, the charge transport capability strongly depends on high quality OSC films with few defects and traps[19, 20]. Considering the structure anisotropy of C8-BTBT derived from its special structure, i.e., two insulating long alkyl groups along axis direction of the BTBT cores and the weak van der Waals (VDW) interactions, the electronic structure and the molecular packing of C8-BTBT is easily affected by the underlying substrates. He et al. fabricated high-quality few-layer C8-BTBT molecular crystals grown on graphene or boron nitride (BN) substrate via VDW epitaxy. It was found that C8-BTBT adopted a lying-down phase at initial stage but a gradual transition to free-standing phase as the thickness increased. The OFETs based on vertical C8-BTBT/ graphene

hetero-structure were confirmed to show excellent performance, while a high field-effect mobility of up to 10 $cm^2V^{-1}s^{-1}$ was obtained in the C8-BTBT/BN-based OFETs[21]. Such phase transition was also observed in Lyu et al.'s studies on C8-BTBT[22, 23], where C8-BTBT is apt to form clusters with disordered orientation on SiO_2 substrate at low coverage of C8-BTBT due to the weak interaction between C8-BTBT and SiO_2. An unconventional downward band bending in C8-BTBT induced by the phase transition of C8-BTBT on HOPG or SiO_2 was also found, which affects the charge transport in C8-BTBT and further affects the performance of C8-BTBT-based OFETs. All works mentioned above provided an important clue on manipulating carrier transport of anisotropic organic molecules similar to C8-BTBT and indicated the importance of the choice of substrates.

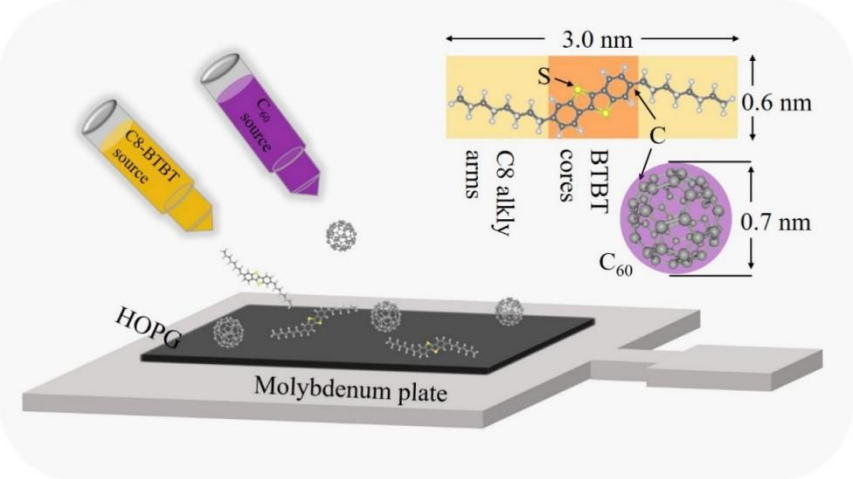

Fig. 1 Schematic diagram of deposition of C_{60} and C8-BTBT molecules on HOPG, the upper right corner inset is the molecular structure of C8-BTBT and C_{60}.

To improve the performance of C8-BTBT-based OFETs, many OSCs have been always introduced to modify the energy level alignment and thus to facilitate charge transport at the interface[19, 20, 24, 25]. Modified by F4-TCNQ layer, solution-crystallized OFETs based on C8-BTBT were reported to deliver a high mobility (3.5-6 $cm^2V^{-1}s^{-1}$) and a low threshold voltage in air[26]. Paterson et al. achieved a hole mobility over 13 $cm^2V^{-1}s^{-1}$ by blending C8-BTBT molecule and conjugated polymer C_{16}IDT-BT[27]. Therefore, the influences of the functional OSC layer on the electronic structure and molecular packing of C8-BTBT/OSCs interface is also of importance and is urging to be further investigated. As an important acceptor material, C_{60} has been extensively used to construct P-N heterojunction with another OSC layer, functionally modifying interfacial energy level alignment, passivating the trap states and even improving the thermal stability of

some small organic molecules[28-34].

In this paper, we studied the modification of a ML C_{60} interlayer on the electronic structure and molecular packing of C8-BTBT on HOPG using X-ray photoelectron spectroscopy (XPS), ultraviolet photoelectron spectroscopy (UPS), atomic force microscopy (AFM) and X-ray diffraction (XRD), etc. The functionalized effect of the introduced C_{60} interlayers was also discussed and some interesting conclusions was drawn. Our work helps to understand the charge transport at C8-BTBT/ OSCs interface and provide an idea to structure C8-BTBT-based OFETs with high performance.

2. Experimental

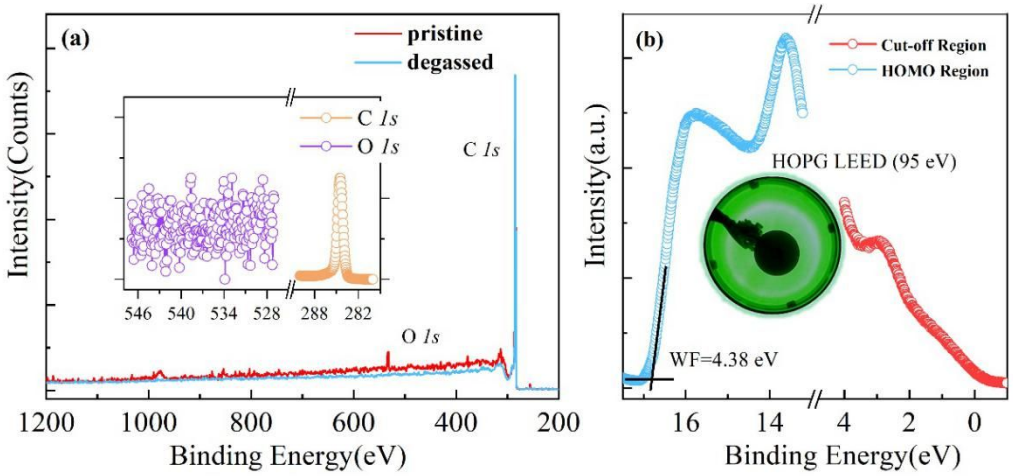

Fig. 2 (a) XPS full-spectrum of pristine and degassed HOPG, the C *1s* and O *1s* core-level spectra of post-degassed HOPG is drawn in the inset. (b) UPS spectra of post-degassed HOPG, the inset is LEED of HOPG.

Sample preparations and photoelectron spectroscopy (PES) were carried out in multiple ultra-high-vacuum chamber which include a spectrometer chamber (base pressure $<1\times10^{-10}$ mbar), an organic molecular beam chamber (base pressure $< 5\times10^{-9}$ mbar), a load lock chamber (base pressure $< 5\times10^{-8}$ mbar) and a radical distribution chamber (base pressure $< 5\times10^{-9}$ mbar) for interconnection. The HOPG freshly cleaved was degassed for 8 h at 450° in the spectrometer chamber. Shown in Fig. 2 are the XPS spectra of impurities related O *1s* peaks, the UPS spectra and low energy electron diffraction (LEED) pattern of HOPG, which indicates a clean and high quality HOPG substrate. Prior to C8-BTBT deposition, a ultrathin C_{60} film of ~0.7 nm was thermally evaporated on HOPG by organic molecular beam epitaxy. It is worth mentioning that

the thickness here obtained by a Quartz Crystal Microbalance (QCM) is an average thickness based on film mass, which should be understood as a "nominal thickness" of C_{60}. Subsequently, the C8-BTBT layer with final thickness of 6.4 nm was deposited layer by layer on the HOPG substrate in the same chamber. The deposition rate of C_{60} and C8-BTBT was precisely controlled at 0.15 and 0.13 nm/ min, respectively, which was monitored by a QCM. The schematic diagram of deposition of C8-BTBT and C_{60} molecules is shown in Fig. 1. The details have been documented in our previous works[35-38].

Thereafter, the XPS and UPS of the prepared samples were collected in the spectrometer chamber in situ. For XPS measurement, the X-ray source was operated at 100 W with 40 eV pass energy and 100 meV step size. For UPS measurement, the UV light spot diameter is about 1 mm and the energy resolution is about 70 meV obtained from the Fermi edge of clean Au (111). The secondary cut-off edge was recorded with sample bias at -5 V. The angle between the incident photon and the emitted photoelectron direction was 45° for both XPS and UPS. The binding energies (E_B) of all spectra were calibrated to the Fermi level (E_F) of the energy analyzer. LEED images were acquired using rear view four grid system (SPECS ErLEED 1000A). X-ray diffraction (Rigaku D. Max 2500 diffractometer. Cu Kα radiation, λ=1.5418 Å) was utilized to identify the out-of-plane crystalline phases of the samples. Using silicon probes with 10 nm curvature radius, AFM measurements were carried out in the tapping mode for organic semiconductor films imaging[39, 40]. XRD and AFM measurements were performed in air conditions. All the measurements were performed at room temperature.

3. Results and discussions

The XPS spectra of C *1s* and S *2p* as a function of the C8-BTBT coverlayer thickness are presented in Fig. 3, in which the CasaXPS was used for Gaussian fitting of C *1s* curves and S *2p* curves [41, 42]. For better visual comparison, all XPS and UPS spectra in Fig. 3 were normalized to unit intensity. The C *1s* peak was consisted of three components associated with the carbon element from HOPG substrate, C_{60} interlayer and C8-BTBT, labeled as C *1s*(HOPG), C *1s*(C_{60}) and C *1s*(C8-BTBT), respectively. The XPS spectra of S *2p* consist of two main peaks attributed to S $2p_{1/2}$ and S $2p_{3/2}$ with fixed energy difference (1.18 eV) , fixed ratio of intensity (2:1) and same full width at half maximal (FWHM, 1.52 eV). All peak positions are marked with vertical

black short solid lines. As shown in Fig. 3a, there is almost no shift of C *1s*(HOPG) with the initial deposition of 0.7 nm C_{60} on HOPG and the further deposition of up to 6.4 nm C8-BTBT on C_{60}/ HOPG. While, a distinguishable shift of about 0.08 eV toward higher binding energy (BE) for C *1s*(C_{60}) occurs with the 0.2 nm C8-BTBT deposition. Then the C *1s*(C_{60}) peak as well as the C *1s*(C8-BTBT) peak moves toward higher BE with the increase of C8-BTBT coverage, delivering a total shift of 0.14 and 0.33 eV for C *1s*(C_{60}) and C *1s*(C8-BTBT), respectively, with a final deposition of 6.4 nm C8-BTBT. At this stage of thick C8-BTBT coverlayer, C *1s* signals attributed to HOPG and C_{60} are much too weak to be distinguished. As for S *2p* spectra in Fig. 3b, a similar shift toward higher BE with C *1s*(C8-BTBT) is also found, achieving a shift of 0.29 eV, slightly smaller than that of C *1s*(C8-BTBT). Interestingly, the shift of C *1s*(C_{60}) occurs just near the C8-BTBT/C_{60} interface region while the shift of C *1s*(C8-BTBT) exists at whole region.

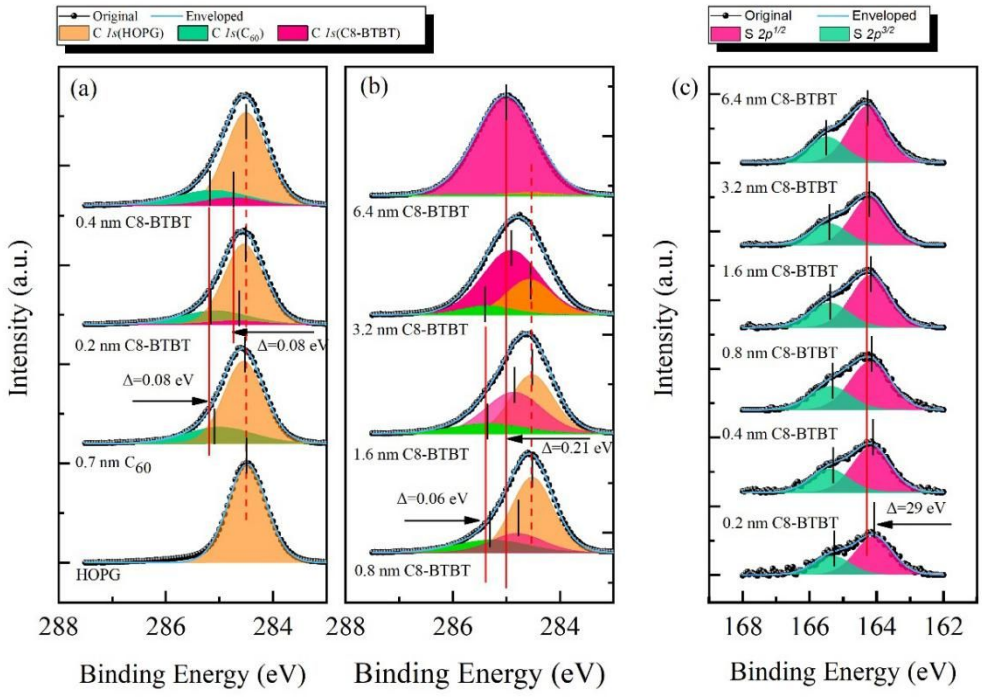

Fig. 3 Thickness dependence XPS core-level spectra of (a) and (b) C *1s* and (c) S *2p* in C8-BTBT, the C *1s* peak is fitted with C *1s*(HOPG), C *1s*(C_{60}) and C *1s*(C8-BTBT), the S *2p* peak is fitted with S $2p^{1/2}$ and S $2p^{3/2}$.

Shown in Fig. 4a are the UPS spectra of secondary electron cut-off edge, from which we can obtain the work function (WF) according to the formula WF=hν-E_C, where hν is the energy of incident photon and E_C the BE of cut-off onset. Linear extrapolation was adopted to determine the value of E_C as well as high occupied molecular orbital (HOMO) as reported in our previous

works[43]. The WF of post-processed bare HOPG substrate is 4.38 eV, and it shifts to 4.56 eV as 0.7 nm C_{60} deposits on HOPG. Although there is a 0.18 eV difference of WF between C_{60} and HOPG, no charge redistribution occurs at C_{60}/HOPG interface which is supported by the unchanged position of C *1s*(HOPG) peaks. Hereafter, the WF suddenly reduces to 4.28 eV with a deposition of 0.2 nm C8-BTBT on as-prepared 0.7 nm C_{60}/HOPG and then monotonically decreases with the further deposition of C8-BTBT. The WF eventually attenuates to 3.76 eV at 6.4 nm C8-BTBT, comparable to that of bulk-phase C8-BTBT[22].

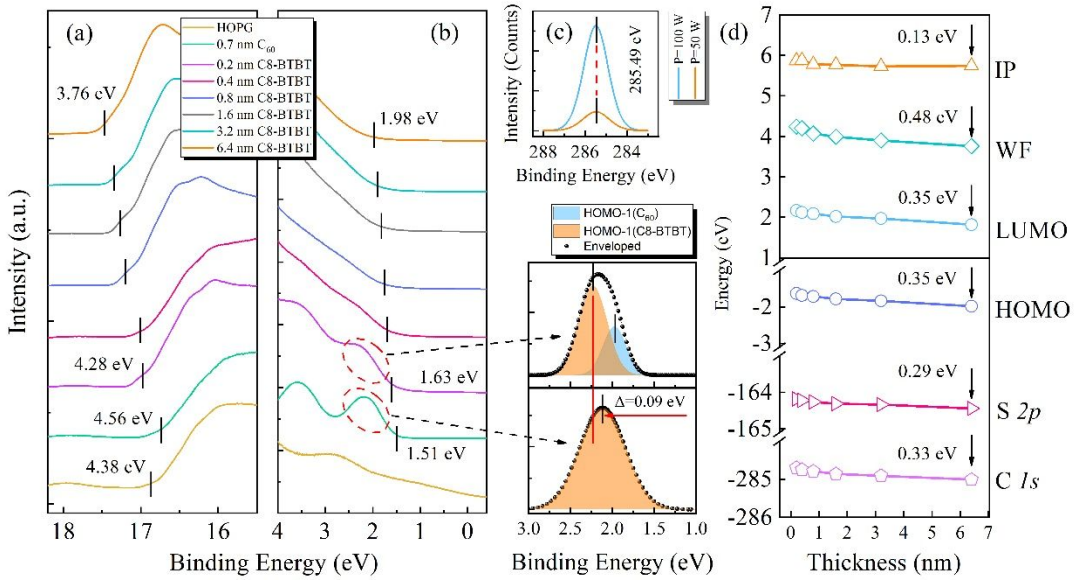

Fig. 4 Thickness dependent UPS spectra of (a) cut-off region and (b) HOMO region; (c) upper panel: XPS core-level spectra of C *1s* for 6.4 nm C8-BTBT/0.7 nm C_{60}/HOPG with X-ray source modulated at 100 W and 50 W, respectively, lower panel: the Gaussian fitting of HOMO with HOMO-1(C_{60}) and HOMO-1(C8-BTBT); (d)the evolution of S *2s*, HOMO, WF and IP with increasing C8-BTBT coverage.

The evaporation thickness dependent HOMO values are presented in Fig. 4b. The HOMO is 1.51 eV upon the deposition of 0.7 nm C_{60}, and two distinct characteristic peaks derived from C_{60} valence band appear at 2.11 eV and 3.59 eV, named as HOMO-1 and HOMO-2 here, respectively. With the following deposition of C8-BTBT, the intensities of the two peaks decrease with an increase in FWHM due to the mingled contribution from C8-BTBT. To distinguish the contributions of C_{60} and C8-BTBT to HOMO, the HOMO-1 peaks for 0.7 nm C_{60}/HOPG and 0.2 nm C8-BTBT/0.7 nm C_{60}/HOPG are fitted with HOMO-1(C_{60}) and HOMO-1(C8-BTBT) after subtracting background as shown in Fig. 3c (the lower panel). The HOMO-1(C_{60}) presents a slight shift of 0.09 eV toward higher BE and the HOMO-1(C8-BTBT) is found to be responsible for the

HOMO onset of the sample which is determined at 1.63 eV. As further increasing the coverage of C8-BTBT, the HOMO onset shows the same shift trend as the cut-off edge with a total shift of 0.35 eV. The HOMO-1(C_{60}) gradually disappears as the increasing thickness of C8-BTBT. However, the HOMO-1(C8-BTBT) is also found to vanish at high coverage of C8-BTBT which seems contradictory with the increasing thickness of C8-BTBT. In fact, the HOMO-1(C8-BTBT) peak is supposed to associate with the lying-down phase of C8-BTBT and the gradual transition to its standing-up phase causes the disappearance of HOMO-1(C8-BTBT) as increasing the coverage of C8-BTBT[44].

To acquire an intuitive image on the change of all energy levels, the thickness dependent evolution of C *1s*, S *2p*, HOMO, low unoccupied molecular orbital (LUMO), WF and ionization potential (IP) of C8-BTBT are plotted in Fig. 4d. The band gap of C8-BTBT is taken as 3.84 eV[45]. Obviously, as the thickness of C8-BTBT increases, C *1s*, S *2p*, HOMO and LUMO present an almost same downward shift of ~0.35 eV, while WF shows a bigger shift of about 0.48 eV which leads to an IP decrease of ~ 0.13 eV. To ensure the observed energy level shifts toward higher BE being exclusively ascribed to the nature of samples, charging effects need to be ruled out here, which often happens in PES tests for many organic semiconductors with poor conductivity. To this end, in Fig. 3c (the upper panel) we present the C *1s* spectra of the 6.4 nm C8-BTBT/0.7 nm C_{60}/HOPG interface with different X-ray source power. If there is charging effect at this sample, the excited photoelectron numbers should certainly depend on the power of X-ray source, which will induce a different energy level shift toward higher BE. Fortunately, the nearly same position of C *1s* peak with 50 W and 100 W X-ray sources excludes the possibility of charging effect most likely due to the excellent conductivity of C8-BTBT. In fact, such an unconventional decrease of IP may be ascribed to phase transition of π-conjugated molecules with structure anisotropy, as reported in previous studies on C8-BTBT/HOPG(SiO_2) and other cases involving 6T, DH6T and CuPc[46, 47]. The interface dipole from different oriented layer of C8-BTBT causes the band bending of C8-BTBT and the C-H surface dipole in the upper layer accounts for the decrease of IP. However, some interesting difference exhibits and remains unclear here owing to an additional insertion of 0.7 nm C_{60} between C8-BTBT and HOPG. More efforts will be carried out to elaborate the electronic structure and the molecular packing mode of the C8-BTBT/0.7 nm C_{60}/HOPG interface.

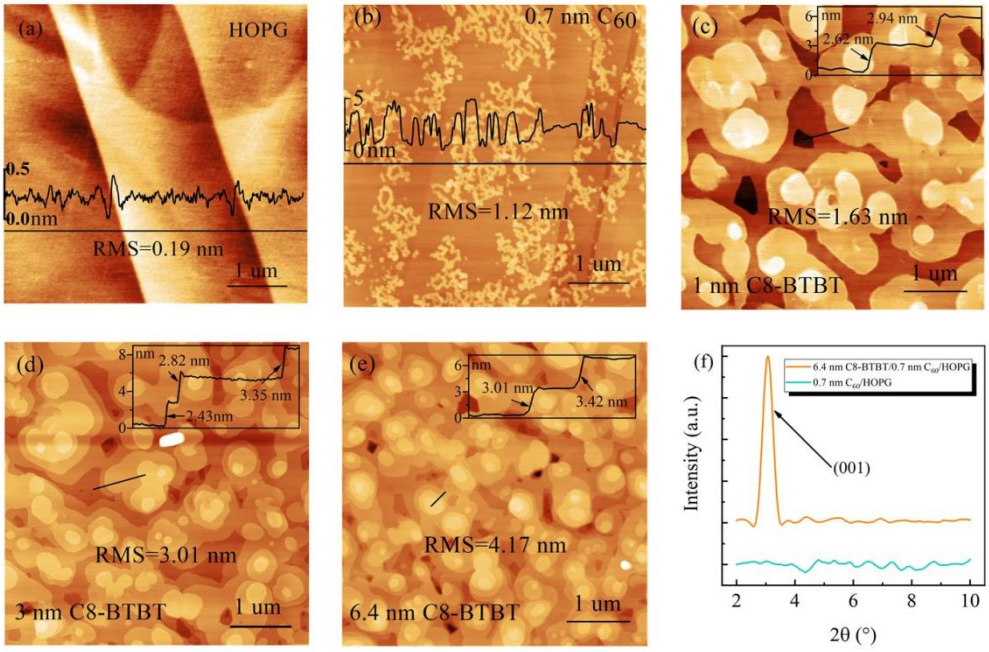

Fig. 5 AFM morphology images (5 μm ×5 μm) of (a) HOPG, (b) 0.7 nm C_{60} on HOPG and (c) 1 nm C8-BTBT, (d) 3 nm C8-BTBT, (e) 6.4 nm C8-BTBT on 0.7 nm C_{60}/HOPG; (f) out-of-plane XRD spectra of 0.7 nm C_{60}/HOPG interface and 6.4 nm C8-BTBT/0.7 nm C_{60}/HOPG interface.

To verify the molecular packing of C8-BTBT on 0.7 nm C_{60}/HOPG, morphology images of HOPG, 0.7 nm C_{60} and different coverage of C8-BTBT were characterized by AFM as shown in Fig. 5a-5e. The root mean square (RMS) of processed HOPG is measured to be as low as 0.19 nm in Fig. 5a and the cross section along the black line shows a height variation of no more than 0.5 nm, indicating that a high quality HOPG substrate with atomically smooth is obtained and it may minimize the impacts of substrate on the overlayers in our research. As a 0.7 nm C_{60} layer is deposited on HOPG, many formed C_{60} clusters are unevenly distributed on the HOPG substrate with a considerable exposure of the underlying substrate. The average height of the clusters far exceeds 0.7 nm as confirmed by the height distribution of C_{60} along the line in Fig. 5b, so the 0.7 nm C_{60}/HOPG configuration delivers a relatively big RMS of 1.12 nm. As show in the inset of Fig. 1, owing to the structure anisotropy of C8-BTBT, it is easy to examine the packing orientation of C8-BTBT molecules from AFM measurements. In Fig. 5c, with the deposition of 1 nm C8-BTBT, several layers of C8-BTBT form on the underlying layer with some large-size islands and an RMS of 1.63 nm. With the deposition of more C8-BTBT molecules, the separated islands gradually coalesce together and form new continuous layers, and new C8-BTBT islands form on the upper layer at the same time, from which we should infer that C8-BTBT molecules grow on 0.7 nm

C_{60}/HOPG in a V-W growth mechanism of as shown in Fig. 5d and 5e.

From the cross section along the black line in Fig. 5c-5e, the evolution of layer height of C8-BTBT layer is described. We can clearly see that the terrace height of C8-BTBT increases with the increasing coverage of C8-BTBT and the step height is about 3.42 nm with the deposition of 6.4 nm C8-BTBT, which is identical to the height of standing orientation C8-BTBT molecules. As expected, the C8-BTBT molecules will eventually relax to a standing-up phase regardless of their initial phase induced by the underlying substrate. The increasing layer height of C8-BTBT means that a phase transition in orientation of C8-BTBT molecules occurs during the relaxation process. However, the least height of terrace measured here is 2.42 nm which is much larger than the height of completely lying-down C8-BTBT molecules. Therefore, the molecular packing of C8-BTBT on 0.7 nm C_{60}/HOPG is not completely figured out here, especially at low coverage of C8-BTBT molecules. The out-of-line XRD was also performed to characterize the crystallinity and crystal orientation of C8-BTBT film as shown in Fig. 5f. Compared to that without deposition of C8-BTBT, a new peak at ~ 3° was observed for the 6.4 nm C8-BTBT/0.7 nm C_{60}/HOPG. The peak is assigned as (001) Bragg reflection of C8-BTBT with a d-spacing of about 3.02 nm. The strong reflection peak implies the high crystallinity of 6.4 nm C8-BTBT on 0.7 nm C_{60}/HOPG and indicates a highly ordered standing-up phase of C8-BTBT at this coverage.

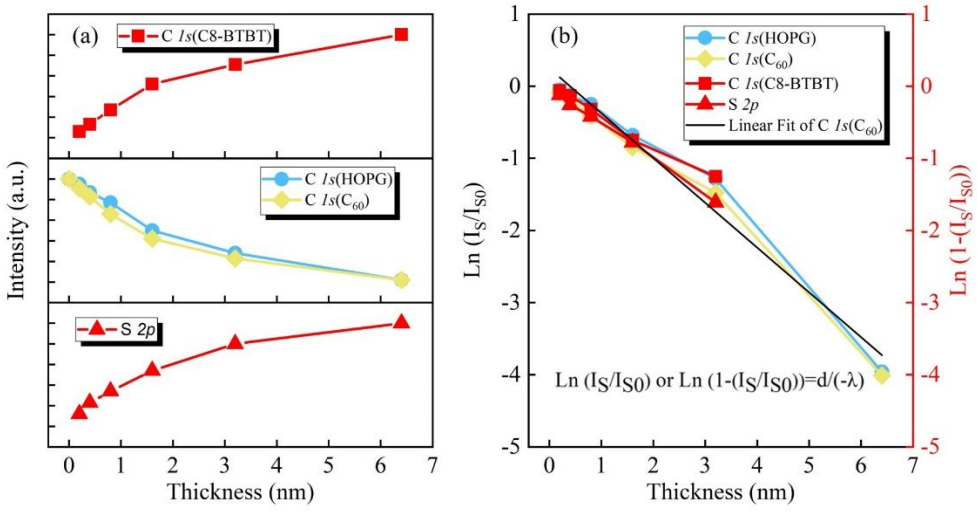

Fig 6. (a) The intensity evolution of C *1s* and S *2p* peaks with increasing C8-BTBT thickness, (b) the depedence of ln (I_S/I_{S0}) or ln (1- I_S/I_{S0}) on the C8-BTBT thickness, I_S and I_{S0} are the peak intensity with and without coverage of C8-BTBT molecules.

The C8-BTBT thickness dependent intensity evolution of XPS core-level spectra in the C8-BTBT layer and the underlying C_{60} and HOPG layers in Fig. 6 provides a further insight on the film growth mode of C8-BTBT on 0.7 nm C_{60}/HOPG. As reported in our previous work, the decreasing peak intensity of the elements in substrate and the increasing peak intensity of those in overlayer will exponentially change with the overlayer thickness as the molecules are deposited on the substrate layer by layer, which can be described by the formula: $I_S=I_{S0}e^{-d/\lambda}$, and $I_S=I_{S0}(1-e^{-d/\lambda})$, respectively, where λ is the mean free path (MFP) of the electron cross the coverage layer and d the thickness of coverage[48, 49]. Apparently, the intensities of C *1s*(HOPG) and C *1s*(C_{60}), C *1s*(C8-BTBT) and S *2p* perfectly agree the formulas above. To further analyze intensity evolution, the normalized intensities as a function of thickness are plotted in Fig. 6b. The intensities of C *1s*(HOPG) and C *1s*(C_{60}) share a similar slope change. The linear fit of C *1s*(C_{60}) is presented and an electron MFP of ~ 2.16 nm is achieved which conforms to normal values among organic semiconductor materials. Interestingly, a slight increase of the absolute value of the C *1s*(C_{60}) slope is observed with increasing the C8-BTBT thickness, which may serve as an other evidence of the V-W growth mode of C8-BTBT on the 0.7 nm C_{60}/HOPG substrate. The formation of C8-BTBT clusters at its low coverage leaves a larger exposure of the underlying C_{60} layer than an evenly distributed C8-BTBT film, so the photoelectron intensity associated with the C *1s*(C_{60}) decreases gently at first. Then the coalescence of C8-BTBT islands leaves a less exposure of the underlying C_{60} layer and leads to a quicker intensity attenuation of photoelectrons.

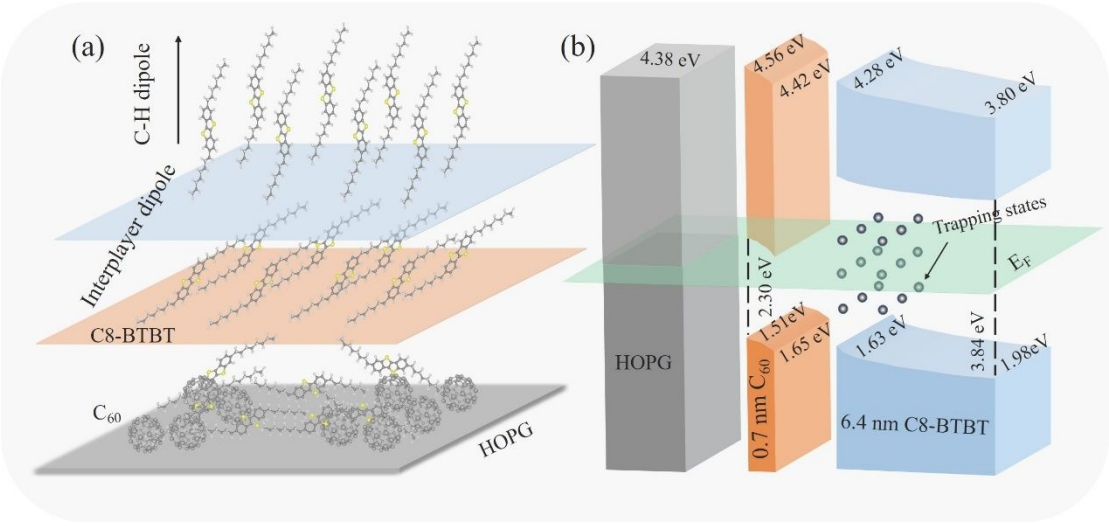

Fig. 7 Schematic drawing of (a) molecular packing and (b) energy level alignment for C8-BTBT

on 0.7 nm C_{60}/HOPG.

Based on the XPS and UPS data, we have inferred a phase transition from the lying-down orientation to the standing-up orientation for the C8-BTBT molecules but remain the molecular orientation of C8-BTBT at initial coverage stage unclear. Compared to C8-BTBT directly deposited on HOPG, we found the HOMO value at low coverage C8-BTBT for C8-BTBT deposited on 0.7 nm C_{60}/HOPG is apparently larger and the decrease value of WF, HOMO, C *1s*, S *2p* and IP is much smaller which probably means the C8-BTBT molecules are not lying completely flat on HOPG at initial stage because the π-π interaction between C8-BTBT and HOPG is not completely propagated by the ultrathin C_{60} interlayer[23]. Further evidences are provided by the AFM characterization. Shown in Fig. 7a is the schematic of molecular packing of C8-BTBT on 0.7 nm C_{60}/HOPG. The step height of 2.42 nm in Fig. 5c indicates that C8-BTBT molecules adopt a lying-down orientation with a big tilt-up angle under the low C8-BTBT coverage. Compared to the case without the 0.7 nm C_{60} interlayer, in which C8-BTBT molecules present an approximately complete lying-down orientation just with some slight disorder, the big tilt-up angle here can be ascribed to the disordered effect derived from the C_{60} interlayer. The step height of 3.42 nm is associated with the standing-up orientation of the C8-BTBT molecules under the high C8-BTBT coverage.

The energy level alignment of 6.4 nm C8-BTBT/0.7 nm C_{60}/HOPG is presented in Fig. 7b, in which the E_g of C_{60} is taken as 2.3 eV here[50]. Owing to negligible difference of WF between C_{60} and HOPG, no charge transport occurs and no dipole forms at the 0.7 nm C_{60}/HOPG interface, hence band bending behavior is not observed at C_{60} side near the interface. At the C8-BTBT/C_{60} interface, an interface dipole of 0.14 eV pointing from C8-BTBT to C_{60} is observed due to electron transport from C8-BTBT region to C_{60} region caused by the WF difference between C8-BTBT and C_{60}. So, a downward band bending in C_{60} layer happens naturally near the interface. The WF of 0.7 nm C_{60} measured here is much smaller than the bulk-phase C_{60} as our previous work[31, 51], most likely due to the contributions from the HOPG substrate considering the evenly distributed C_{60} on HOPG without a complete coverage[52, 53]. For the C8-BTBT side, a noticeable downward band bending is also found, which induces a built-in field and thus a p-doped surface state region. Both the charge transfer at C8-BTBT/C_{60} interface and the orientation transition of C8-BTBT contribute to the downward band bending of C8-BTBT. However, the former always occurs at the very near interface, while the latter seems to occur farther away from the interface as supported by the minor decrease of IP near the interface.

A strong hole accumulation near this interface may facilitate the formation of high concentration conducting channel as this interface is incorporated into organic device. In addition, combined with the band bending of C8-BTBT and C_{60}, the HOMO difference between C8-BTBT and C_{60} is greatly reduced which means a smaller hole barrier forms at the interface for hole transport from C8-BTBT to HOPG. At the same time, the LUMO difference between C8-BTBT and C_{60} increases at the very near interface region which enlarges the electron barrier for electron transport from C_{60} to C8-BTBT and reduces the possibility of electron-hole recombination at the interface. Lastly, the LUMO of C_{60} resides in the gap of C8-BTBT owing to the wide gap of C8-BTBT, and the trap states derived from the defects in C8-BTBT can be greatly passivated after the in-gap trap states above the level of the HOMO are filled, which can deliver a weak hysteresis effect and a small threshold voltage in related devices. Therefore, the insertion of 0.7 nm C_{60} is expected to improve the performance of C8-BTBT-based devices with low threshold voltage and higher mobility. Our results deduce that the C8-BTBT films modified by ultrathin C_{60} interlayer have great potential in organic electronic device filed.

4. Conclusions

In summary, the electronic structure and the molecular packing mode of the C8-BTBT/0.7 nm C_{60}/HOPG interface have been investigated by XPS, UPS, AFM and XRD characterization. C8-BTBT molecules grow on 0.7 nm C_{60}/HOPG in a V-W mode and the π-π interaction between C8-BTBT and HOPG is weakened by the thin C_{60} interlayer to some extent which make the C8-BTBT molecules still adopt a lying-down orientation at low coverage but with a tilt angel. The tilt up C8-BTBT layer owns a bigger HOMO than the completely lying-down ones. A downward band bending occurs in both C8-BTBT and C_{60} layer at the C8-BTBT/C_{60} interface due to the carrier transfer together with the phase transition in C8-BTBT. The HOMO of C8-BTBT near the interface is largely lifted up by the C_{60} insertion layer which cause a p-doping effect and an increase of hole mobility in C8-BTBT. The hole transfer barrier at the interface is largely reduced while electron transfer barrier is clearly increased. Owing to the wide gap of C8-BTBT, the LUMO of C_{60} residing in gap of C8-BTBT can probably passivate the trapping states in C8-BTBT. Our efforts help to better understand the electron structure and film growth of anisotropy molecules and provide a useful strategy to improve performance of C8-BTBT-based devices.

Acknowledgements

This work was supported by the National Natural Science Foundation of China (Grant No. 51673217) and the Fundamental Research Funds for the Central South University (502221903). Y. Gao acknowledges the support of the National Science Foundation (Grant No. DMR-1903962).

References

1 J. Xu, H. C. Wu, C. Zhu, A. Ehrlich, L. Shaw, M. Nikolka, S. Wang, F. Molina-Lopez, X. Gu, S. Luo, D. Zhou, Y. H. Kim, G. N. Wang, K. Gu, V. R. Feig, S. Chen, Y. Kim, T. Katsumata, Y. Q. Zheng, H. Yan, J. W. Chung, J. Lopez, B. Murmann and Z. Bao, *Nat. Mater*, 2019, **18**, 594-601.

2 S. E. Root, S. Savagatrup, A. D. Printz, D. Rodriquez and D. J. Lipomi, *Chem. Rev*, 2017, **117**, 6467-6499.

3 T. Sekitani, H. Nakajima, H. Maeda, T. Fukushima, T. Aida, K. Hata and T. Someya, *Nat Mater*, 2009, **8**, 494-499.

4 S. T. Lee, Y. M. Wang, X. Y. Hou and C. W. Tang, *Appl. Phys. Lett.*, 1999, **74**, 670-672.

5 C. Zhang, P. Chen and W. Hu, *Chem. Soc. Rev*, 2015, **44**, 2087-2107.

6 H. Sirringhaus, *Adv. Mater*, 2014, **26**, 1319-1335.

7 J. W. Shi, H. B. Wang, D. Song, H. K. Tian, Y. H. Geng and D. H. Yan, *Adv. Func. Mater*, 2007, **17**, 397-400.

8 C. W. Tang, *Appl. Phys. Lett.*, 1986, **48**, 183-185.

9 J. Wang, S. Luo, Y. Lin, Y. Chen, Y. Deng, Z. Li, K. Meng, G. Chen, T. Huang, S. Xiao, H. Huang, C. Zhou, L. Ding, J. He, J. Huang and Y. Yuan, *Nat. Commun*, 2020, **11**, 582.

10 C. Barraud, P. Seneor, R. Mattana, S. Fusil, K. Bouzehouane, C. Deranlot, P. Graziosi, L. Hueso, I. Bergenti, V. Dediu, F. Petroff and A. Fert, *Nat. Phys*, 2010, **6**, 615-620.

11 M. Cinchetti, V. A. Dediu and L. E. Hueso, *Nat. Mater*, 2017, **16**, 507-515.

12 H. Ebata, T. Izawa, E. Miyazaki, K. Takamiya, M. Ikeda, H. Kuwabara and T. Yui, *J. Am. Chem. Soc.*, 2007, **129**.

13 Y. Tsutsui, G. Schweicher, B. Chattopadhyay, T. Sakurai, J. B. Arlin, C. Ruzie, A. Aliev, A. Ciesielski, S. Colella, A. R. Kennedy, V. Lemaur, Y. Olivier, R. Hadji, L. Sanguinet, F. Castet, S. Osella, D. Dudenko, D. Beljonne, J. Cornil, P. Samori, S. Seki and Y. H. Geerts, *Adv. Mater.*, 2016, **28**, 7106-7114.

14 H. Minemawari, T. Yamada, H. Matsui, J. Tsutsumi, S. Haas, R. Chiba, R. Kumai and T. Hasegawa, *Nature*, 2011, **475**, 364-367.

15 Y. Yuan, G. Giri, A. L. Ayzner, A. P. Zoombelt, S. C. Mannsfeld, J. Chen, D. Nordlund, M. F. Toney, J. Huang and Z. Bao, *Nat. Commun*, 2014, **5**, 3005.

16 D. He, J. Qiao, L. Zhang, J. Wang, J. Xu and W. X., *Sci. Adv*, 2017, **3**, 9.

17 S. Tong, J. Sun, C. Wang, Y. Huang, C. Zhang, J. Shen, H. Xie, D. Niu, S. Xiao, Y. Yuan, J. He, J. Yang and Y. Gao, *Adv. Electron. Mater*, 2017, **3**. 1700058.

18 J. Tsurumi, H. Matsui, T. Kubo, R. Häusermann, C. Mitsui, T. Okamoto, S. Watanabe and J. Takeya, *Nat. Phys*, 2017, **13**, 994-998.

19 K. Zhang, N. B. Kotadiya, X. Y. Wang, G. J. A. H. Wetzelaer, T. Marszalek, W. Pisula and P. W. M. Blom, *Advanced Electronic Materials*, 2020, DOI: 10.1002/aelm.201901352.

20 N. Koch, *Chemphyschem*, 2007, **8**, 1438-1455.

21 D. He, Y. Zhang, Q. Wu, R. Xu, H. Nan, J. Liu, J. Yao, Z. Wang, S. Yuan, Y. Li, Y. Shi, J. Wang, Z. Ni, L. He, F. Miao, F. Song, H. Xu, K. Watanabe, T. Taniguchi, J. B. Xu and X. Wang, *Nat. Commun*, 2014, **5**, 5162.

22 L. Lyu, D. Niu, H. Xie, Y. Zhao, N. Cao, H. Zhang, Y. Zhang, P. Liu and Y. Gao, *Phys. Chem. Chem. Phys*, 2017, **19**, 1669-1676.

23 L. Lyu, D. Niu, H. Xie, N. Cao, H. Zhang, Y. Zhang, P. Liu and Y. Gao, *J. Chem. Phys*, 2016, **144**, 034701.

24 S. Lach, A. Altenhof, K. Tarafder, F. Schmitt, M. E. Ali, M. Vogel, J. Sauther, P. M. Oppeneer and C. Ziegler, *Adv. Funct. Mater.*, 2012, **22**, 989-997.

25 X. Liu, Q. Han,Y. Liu, C. Xie, C. Yang, D. Niu, Y. Li, H. Wang, L. Xia, Y. Yuan, and Y. Gao, *Appl. Phys. Lett*., 2020, **116**, 253303.

26 J. Soeda, Y. Hirose, M. Yamagishi, A. Nakao, T. Uemura, K. Nakayama, M. Uno, Y. Nakazawa, K. Takimiya and J. Takeya, *Adv. Mater*, 2011, **23**, 3309-3314.

27 A. F. Paterson, N. D. Treat, W. Zhang, Z. Fei, G. Wyatt-Moon, H. Faber, G. Vourlias, P. A. Patsalas, O. Solomeshch, N. Tessler, M. Heeney and T. D. Anthopoulos, *Adv. Mater.*, 2016, **28**, 7791-7798.

28 C. Fan, A. P. Zoombelt, H. Jiang, W. Fu, J. Wu, W. Yuan, Y. Wang, H. Li, H. Chen and Z. Bao, *Adv. Mater*, 2013, **25**, 5762-5766.

29 T. D. Ibragimov, A. R. Imamaliyev and G. F. Ganizade, *Mol. Cryst. Liq. Cryst.*, 2019, **691**, 27-34.

30 H. Li, C. Fan, W. Fu, H. L. Xin and H. Chen, *Angew. Chem. Int. Ed. Engl*, 2015, **54**, 956-960.

31 X. Liu, C. Wang, C. Wang, I. Irfan and Y. Gao, *Org. Electron*, 2015, **17**, 325-333.

32 S. Olthof, S. Singh, S. K. Mohapatra, S. Barlow, S. R. Marder, B. Kippelen and A. Kahn, *Appl. Phys. Lett*, 2012, **101**. 253303.

33 X. H. Zhang and B. Kippelen, *Appl. Phys. Lett*, 2008, **93**. 133305.

34 X. Liu, S. Yi, C. Wang, C. Wang and Y. Gao, *J. Appl. Phys*, 2014, **115**. 163708.

35 P. Liu, X. Liu, L. Lyu, H. Xie, H. Zhang, D. Niu, H. Huang, C. Bi, Z. Xiao, J. Huang and Y. Gao, *Appl. Phys. Lett*, 2015, **106**. 193903.

36 Y. Liu, C. Xie, W. Tan, X. Liu, Y. Yuan, Q. Xie, Y. Li and Y. Gao, *Org. Electron.*, 2019, **71**, 123-130.

37 W. Tan, C. Xie, Y. Liu, Y. Zhao, L. Li, X. Liu, Y. Yuan, Y. Li and Y. Gao, *Synth. Met.*, 2018, **246**, 101-107.

38 Y. Zhao, X. Liu, L. Lyu, L. Li, W. Tan, S. Wang, C. Wang, D. Niu, H. Xie, H. Huang and Y. Gao, *Synthetic. Met*, 2017, **229**, 1-6.

39 Y. Huang, J. Sun, J. Zhang, S. Wang, H. Huang, J. Zhang, D. Yan and Y. Gao, *Org. Electron*, 2016, **36**, 73.

40 S. Wang, L. Lyu, D. Niu, L. Zhang, H. Huang and Y. Gao, *Appl. Phys. Lett.*, 2019, **114**. 241602.

41 L. Li, C. Wang, C. Wang, S. Tong, Y. Zhao, H. Xia, J. Shi, J. Shen, H. Xie, X. Liu, D. Niu, J. Yang, H. Huang, S. Xiao, J. He and Y. Gao, *Org. Electron.*, 2019, **65**, 162-169.

42 H. Xie, D. Niu, L. Lyu, H. Zhang, Y. Zhang, P. Liu, P. Wang, D. Wu and Y. Gao, *Appl. Phys. Lett.*, 2016, **108**, 034701.

43 X. Liu, C. Wang, Irfan, S. Yi and Y. Gao, *Org. Electron.*, 2014, **15**, 977-983.

44 S. Wang, D. Niu, L. Lyu, Y. Huang, X. Wei, C. Wang, H. Xie and Y. Gao, *Appl. Sur. Sci*. 2017, **416**, 696–703.

45 H. Kobayashi, N. Kobayashi, S. Hosoi, N. Koshitani, D. Murakami, R. Shirasawa, Y. Kudo, D. Hobara, Y. Tokita and M. Itabashi, *J. Chem. Phys*, 2013, **139**, 014707.

46 W. Chen, H. Huang, S. Chen, X. Gao and T. S. W. Andrew, *J. Phys. Chem. C*, 2008, **112**, 5037.

47 S. Duhm, G. Heimel, I. Salzmann, H. Glowatzki, R. L. Johnson, A. Vollmer, J. P. Rabe and N. Koch, *Nat. Mater*, 2008, **7**, 326-332.

48 M. Zhu, L. Lyu, D. Niu, H. Zhang, Y. Zhang, P. Liu and Y. Gao, *Appl. Surf. Sci.*, 2017, **402**, 142-146.

49 H. Xie, D. Niu, Y. Zhao, S. Wang, B. Liu, Y. Liu, H. Huang, P. Wang, D. Wu and Y. Gao, *Synth. Met.*, 2020, **260**. 116261.

50 R. W. Lof, M. A. van Veenendaal, B. Koopmans, H. T. Jonkman and G. A. Sawatzky, *Phys. Rev. Lett*, 1992, **68**, 3924-3927.

51 C. Wang, D. Niu, S. Wang, Y. Zhao, W. Tan, L. Li, H. Huang, H. Xie, Y. Deng and Y. Gao, *J. Phys. Chem. Lett*, 2018, **9**, 5254-5261.

52 M. Gobbi, L. Pietrobon, A. Atxabal, A. Bedoya-Pinto, X. Sun, F. Golmar, R. Llopis, F. Casanova and L. E. Hueso, *Nat. Commun*, 2014, **5**, 4161.

53 S. Hietzschold, S. Hillebrandt, F. Ullrich, J. Bombsch, V. Rohnacher, S. Ma, W. Liu, A. Kohn, W. Jaegermann, A. Pucci, W. Kowalsky, E. Mankel, S. Beck and R. Lovrincic, *ACS Appl. Mater. Inter*, 2017, **9**, 39821-39829.

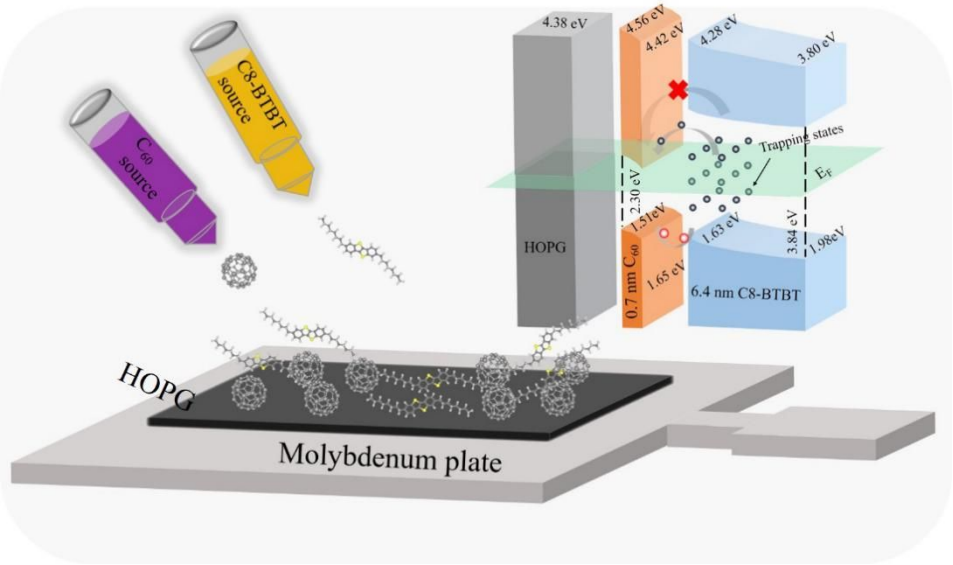
C60 source
C8-BTBT source
HOPG
Molybdenum plate
4.38 eV
4.56 eV
4.42 eV
4.28 eV
3.80 eV
Trapping states
EF
2.30 eV
1.51eV
1.63 eV
3.84 eV
1.98eV
0.7 nm C60
1.65 eV
6.4 nm C8-BTBT

TOC